

The X-ray spectrum of δ Orionis observed by *LETGS* aboard *Chandra*

A.J.J. Raassen^{1,2} and A.M.T. Pollock³

¹ SRON Netherlands Institute for Space Research, Sorbonnelaan 2, 3584 CA Utrecht, The Netherlands

² Astronomical Institute "Anton Pannekoek", Science Park 904, 1098 XH Amsterdam, University of Amsterdam, The Netherlands

³ European Space Agency XMM-Newton Science Operations Centre, European Space Astronomy Centre, Apartado 78, Villanueva de la Cañada, 28691 Madrid, Spain

26 November 2012

ABSTRACT

Aims. We analyze the high-resolution X-ray spectrum of the supergiant O-star δ Orionis (O9.5II) with line ratios of He-like ions and a thermal plasma model, and we examine its variability.

Methods. The O-supergiant δ Ori was observed in the wavelength range 5–175 Å by the X-ray detector HRC-S in combination with the grating LETG aboard *Chandra*. We studied the He-like ions in combination with the UV-radiation field to determine local plasma temperatures and to establish the distance of the X-ray emitting ions to the stellar surface. We measured individual lines by means of Gaussian profiles, folded through the response matrix, to obtain wavelengths, line fluxes, half widths at half maximum (HWHM) and line shifts to characterize the plasma. We consider multitemperature models in collisional ionization equilibrium (CIE) to determine temperatures, emission measures, and abundances.

Results. Analysis of the He-like triplets extended to N VI and C V implies ionization stratification with the hottest plasma to be found within a few stellar radii $3 R_*$ (Mg XI) and the coolest farther out, far beyond the acceleration zone, up to $49 R_*$ (N VI) and $75 R_*$ (C V). The observed temperatures cover a range from about 0.1 to 0.7 keV, i.e., 1–8 MK. The X-ray luminosity (L_x) is $\sim 1.5 \times 10^{32}$ erg/s in the range from 0.07 to 3 keV covered by *LETGS*. Velocity widths of about 1040 km s⁻¹ have been determined.

Key words. techniques: spectroscopic – stars: individual: δ Ori – stars: stellar wind stars: early-type – missions: *Chandra*

1. Introduction

Since the launch of the first X-ray observatories, it has been known that O-type stars and early B-type stars are X-ray sources. Harnden et al. (1979), Seward et al. (1979), and Cassinelli et al. (1981) described the first observations with *Einstein*. The investigations were continued with *ASCA* (Corcoran et al. 1994) and *ROSAT* (Haberl & White 1993, Berghöfer et al. 1996). Although the origin of the emission was initially a matter of debate, it is now generally believed that instabilities and clumping in the strong line-driven stellar wind is the mechanism that heats small parts of the wind (e.g., Lucy & Solomon 1970; Lucy & White 1980; Lucy 1982; Owocki et al. 1988; Dessart & Owocki 2005). The launches of *Chandra* and *XMM-Newton* in 1999 with high-resolution instruments aboard have offered the possibility to study the X-ray spectra in more detail, resulting in, e.g., estimates of line ratios, line profiles, temperatures, emission measures, and abundances (Waldron & Cassinelli 2001, 2007; Cohen et al. 2006; Kahn et al. 2001; Raassen et al. 2008). Generally, the overall spectra have been described by means of collisional ionization equilibrium (CIE) models with several temperature components, often complemented by analysis of individual line profiles, line fluxes, and line flux ratios of He-like ions. Based on *RGS* observations of ζ Ori, Pollock (2007) suggests an alternative mechanism due to the non-equilibrium ion-ion interactions far out in the wind. Since extending the high-resolution coverage to the longer wavelengths available with the *Chandra LETGS*

should provide new constraints on theory, it has been proposed to record the spectrum of δ Ori, the softest of the X-ray brightest O-stars observed with *ROSAT*. This paper discusses the *LETGS* data obtained in the context of individual line diagnostics to obtain plasma characteristics, as well as overall thermal models.

The O-star δ Ori (HD 36486) is the western star in the belt of Orion, named Mintaka, with a parallax of 4.71(0.58) mas, i.e., at a distance of 212 pc (SIMBAD: Van Leeuwen 2007)¹. The position in J2000 coordinates is RA=05 32 00.400 and Dec=-00 17 56.74. It is a bright X-ray source and suffers lower interstellar absorption than ζ Ori. It is part of a triple star system, containing of δ OriA, δ OriB, and δ OriC. Here we focus on the “single star” δ OriA, which in itself is also a triple star system (Aa1, Aa2, and Ab). The tertiary star (Ab) is too far away to play a role in our observation. The primary (Aa1), a supergiant, is of spectral type O9.5II, with a temperature of 33000K. The secondary (Aa2) is of spectral type B0.5III, with a temperature of 27000K (Voels et al. 1989 and Tarasov et al. 1995). They form a binary system with a period of 5.7325 days (Harvey et al. 1987). Different stellar mass values are given in the literature. Harvin et al. (2002) give $M_p = 10.3 M_\odot$ as average with $R_p = 11 R_\odot$ and for the secondary star $M_s = 5.2 M_\odot$ and $R_s = 4 R_\odot$, while Mayer et al. (2010) suggest values of $M_p = 25 M_\odot$ with $R_s = 16 - 17 R_\odot$. The primary and secondary stars are separated by $33 R_\odot$, equivalent to $3 R_p$. The properties of δ Ori, which we have applied, are given in Table 1.

The spectrum of δ Ori was studied in X-rays with earlier satellites by Cassinelli & Swank (1983), Haberl & White (1993),

Send offprint requests to: A.J.J. Raassen,
e-mail: a.j.j.raassen@srn.nl

¹ <http://simbad.u-strasbg.fr/simbad/sim-fid>

Table 1. Adopted properties of δ Ori.

Property	δ Ori
Distance from Earth(pc)	212 ^a
Spectral type	O9.5II ^b
Radius(R_{\odot})	11 ^b
Mass(M_{\odot})	10.3 ^b
T_{eff} (K)	33000 ^c
Terminal wind velocity(km s ⁻¹)	2000 ^d
\dot{M} (M_{\odot} yr ⁻¹)	1.07×10^{-6d}

Notes:

a: Van Leeuwen (2007)*b*: Miller et al.(2002), taken from Harvin et al. (2002).*c*: Miller et al.(2002), taken from Voels et al. (1989).*d*: Miller et al.(2002), taken from Lamers & Leitherer (1993).

and Corcoran et al. (1994) and most recently at high resolution by Waldron & Cassinelli (2007) and Miller et al. (2002) with the *Chandra HETGS*. They focused on line profiles and line widths, together with ratios of forbidden and intercombination lines in He-like ions.

The set up of this paper is as follows. The emphasis of the paper is on determining the location of the X-ray emitting plasma and its temperature in relation to the stellar surface and the UV-radiation field. Therefore we need individual line fluxes. In Sect. 2 the observation and the lightcurve are discussed. We show individual line fluxes, line wavelengths, and line broadenings in Sect. 3. Based on the individual line fluxes of He-like ions, the location relative to the stellar surface, as well as the temperature of the plasma, is derived. They are given in Sect. 4. We discuss a multitemperature model fit to the total spectrum with a CIE-model in Sect. 5. As suggested by the light curve, we also make a time split, dividing the total observation of 98 ks into the first part of 49 ks and the second part of 49 ks.

2. Observation and lightcurve

2.1. Data and pipelining

The X-ray spectrum of δ Ori was obtained by means of *HRC-S* in combination with the Low-Energy-Transmission-Grating (*LETG*) on board *Chandra* on November 9, 2007 during 97 ks (JD=54413.92705-54415.05066). The log of the observation is shown in Table 2.

The data were pipelined with CIAO3.4 with CALDB version 3.4.1 and prepared for SPEX by the programs *extract* and *crele* developed at SRON. The spectrum derived from this observation is the sum of the +1 and -1 order. The background, which is quite dominant in the higher wavelength area of *LETG* spectra, has been subtracted. The spectrum contains 31500 counts in the spectral range from 5 to 175 Å.

2.2. Zeroth-order lightcurve

In other wavelength ranges (optical and IUE) fluctuations due to eclipsing have been observed in the lightcurve of δ Ori. These changes are about .12m for the primary eclipse and .07m for the secondary eclipse (Harvin et al. 2002). This corresponds to a decrease of about 11% during the primary eclipse and of about 6% during the secondary eclipse. Based on the zeroth-order image a lightcurve has been constructed. Figure 1 shows the zeroth-order lightcurve of this observation of δ Ori. The total number of

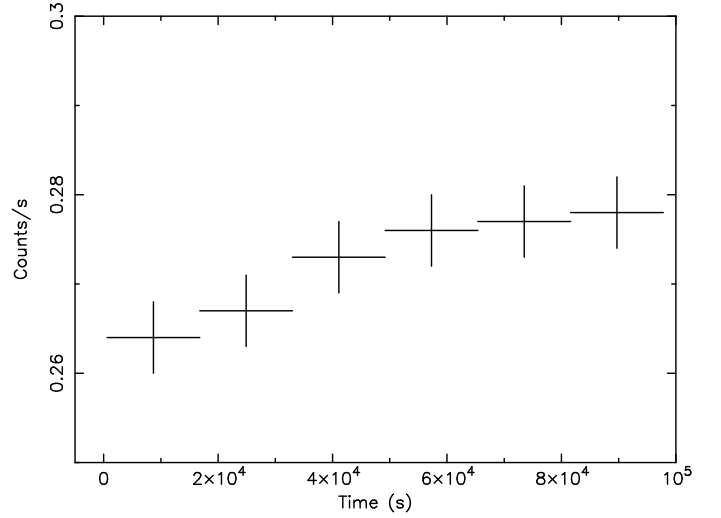


Fig. 1. The zeroth-order lightcurve of δ Ori, observed with *LETGS*, and rebinned to time bins of 15700 seconds. The curve indicates a minimum at the beginning of the observation and a flattening of the increase at the end of the observation.

counts in this zeroth-order image is 26350 counts. No periodicity could be established in the lightcurve, as this observation is too short to cover several stellar revolutions. However, after rebinning to time bins of about 16 ks the lightcurve shows some variation in count rate from 0.264(0.004) to 0.278(0.004) counts/s during this observation. This is a change of about 5%. During the observation the phase of the binary system was 0.83-0.02, derived from Harvin et al. (2002), or 0.87-0.07, as derived from Mayer et al. (2010). This implies that the secondary is in front of the primary during the observation. In later sections we investigate a possible relation between the behavior of the lightcurve and the observed spectrum by cutting the observation into a first part from 0 to 49 ks and a second part from 49 to 98 ks.

3. Individual line fluxes

The individual line fluxes of the *LETGS* spectrum of δ Ori were measured. For each observed line a Gaussian profile was folded through the response matrix and fit to the observed line profile, establishing the line positions, line fluxes, as well as the linewidths. A powerlaw was added to describe the continuum near the line features. The line profiles are symmetric. This is shown in Fig. 2 for the O VIII and C VI lines. This agrees with observations of δ Ori by Miller et al. (2002), when applying *HETGS*. Seeming asymmetries in the data are due to asymmetries in the instrumental line spread function (LSF). It also influences the observed widths of the lines. The situation in ζ Ori is different. In that star the lines are asymmetric and broadened by themselves as shown by Pollock (2007).

The measured wavelengths (Å) and line fluxes (in units 10^{-4} photons cm⁻²s⁻¹ and in units 10^{-13} ergs cm⁻²s⁻¹) are collected in Table 3, together with the theoretical wavelengths from laboratory measurements collected by Kelly (1987) and the *NIST4* database². The stronger lines have a low value for the (1 σ) uncertainty. Their uncertainties are a few mÅ.

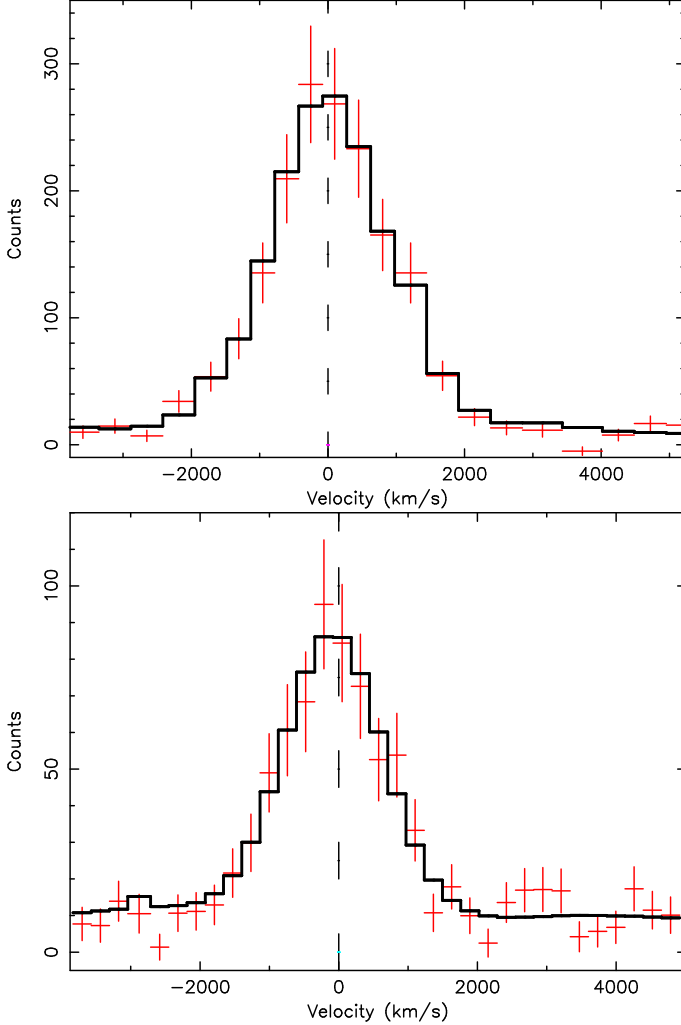
There are very few line features above 50 Å, and they are often due to higher-order lines, especially third-order lines, which have their strong first-order component between 10 and

² <http://www.nist.gov/pml/data/asd.cfm>

Table 2. Observation log of the data of δ Ori.

Obs ID	Instrument	Grating	Start Date	End Date	Duration(ks)	Wavelength range ^a
7416	HRC-S	LETG	2007-11-09T10:14:57 JD 54413.92705	2007-11-10T13:12:57 JD 54415.05066	97.08	5-175 Å

Notes:

^a: Range also used during the fitting procedure.**Fig. 2.** Line shapes of the O VIII line at 18.97 Å and the C VI line at 33.74 Å in the spectrum of δ Ori. Data are in red/gray, the fitted Gaussian model line folded through the response matrix is given in black. The rest wavelength is also shown. Keep in mind that the width is also influenced by the instrumental line spread function.

35 Å. The second-order lines of Fe XVII at 16.777, 17.054, and 17.097 Å contribute a bit to the wings of the C VI line at 33.736 Å. The third-order Ne X resonance line at 12.134 Å is blended by the S XII transition at 36.500 Å, and the second-order O VIII resonance line contributes to the wing of the S XI and Si XIII feature at 37.787 Å. Some free unblended higher-order lines are given in Table 4. The higher order lines are implemented in the model fits of Sects. 5.1 and 5.2. First-order lines in the wavelength range above 50 Å belong to lower ionization stages of sil-

icon and iron, and their optimal ionization temperature is around 0.1 keV.

Some stronger lines are collected in Table 5 and shown in Fig. 3. This table shows the line shifts and the line broadenings. The line shifts show velocities between -160 and +160 km s⁻¹. The earth's orbital velocity in the direction of δ Ori during the observation and the velocity of δ Ori itself (Wilson 1963) are both about 16 km s⁻¹, but they have opposite signs and are canceling. The obtained velocities are comparable with those given by Miller et al. (2002), based on observations by *HETGS*. The HWHMs of the strong lines result in a velocity of about 840 km s⁻¹, below the terminal velocity of 2000 km s⁻¹. Our value is higher than the values given by Miller et al. (2002), based on *HETGS*. This might be due to an inconsistency between the instrumental LSFs of *LETGS* and *HETGS*. However, our value agrees with Wojdowski & Schulz (2005), who also used *HETGS*. The ultimate velocity at the end of the wing, corrected for the instrumental width are also given. These values are about 1850 km s⁻¹ with an uncertainty of 200 km s⁻¹. The lines in the separated spectra obtained from the two time intervals (0-49 ks and 49-98 ks) were measured, and no significant differences between the line measurements of the two time intervals have been established.

4. He-like line ratios

The individual line fluxes of the line triplets in the He-like ions, consisting of a resonance line (r), an intercombination line (i), and a forbidden line (f), are tools for density and temperature diagnostics (Gabriel and Jordan 1969), because the upper level of the forbidden line ($1s2s\ ^3S_1$) is depopulated by collisions in favor of the upper level of the intercombination line ($1s2p\ ^3P_1$). On the other hand, the same effect of depopulation can be caused by a strong UV radiation field (Blumenthal et al. 1972). The latter gives the size of the UV field flux and therewith an indication of the distance to the stellar surface where the X-ray emitting ions are formed. While for late type stars the collisions and therewith the electron density are the dominant processes, for hot, early type stars the strong UV radiation field (the location relative to the stellar surface) is most important. This has become a well-proven diagnostic tool for establishing the radial location of the X-ray source in the stellar wind of hot stars (Miller et al. 2002; Leutenegger et al. 2006; Waldron & Cassinelli 2007). The appropriate features in the He-like ions of C V, N VI, O VII, Ne IX, Mg XI, and Si XIII lie in the range from 5 to 45 Å, which is covered by *LETGS*.

The line fluxes of these special cases have been measured a slightly different way from the other lines given in Table 3. After the final overall multitemperature CIE-model fit (see Sect. 5), limited wavelength ranges were selected just around the relevant line features of the He-like ions. Then the lines from the ions under investigation were ignored from the model. In this way the continuum is based on the multitemperature fit and possible

Table 3. Line positions and line fluxes in δ Ori.

ion	λ_0^a [Å]	λ_{obs}^b [Å]	flux ^c	flux ^d
S xv	5.038+.066	4.977(.103) ^f	0.27(.15)	1.07
Si xiv	6.182	6.168(.029)	0.05(.03)	0.14
Si xiii	6.648	6.635(.007)	0.14(.03)	0.43
Si xiii	6.688+.704	6.698(.011)	0.08(.03)	0.24
Si xiii	6.740	6.751(—)	0.01(.01)	0.03
Mg xii	8.422	8.423(.009)	0.09(.03)	0.21
Mg xi	9.168	9.165(.008)	0.18(.04)	0.39
Mg xi	9.231	9.229(.010)	0.12(.04)	0.25
Mg xi	9.314	9.315(.011)	0.08(.03)	0.17
Ne x	9.710	9.716(.019)	0.08(.04)	0.17
Ne x	10.240	10.238(.012)	0.08(.03)	0.15
Fe xix	10.640	10.647(.008)	0.11(.04)	0.21
Fe xvii	11.130	11.136(.019)	0.05(.03)	0.09
Fe xvii	11.251	11.274(.016)	0.09(.04)	0.16
Fe xviii	11.530	11.552(.009)	0.16(.04)	0.28
Ne x	12.134	12.131(.003)	1.00(.08)	1.66
Fe xxi	12.286	12.271(.008)	0.28(.05)	0.45
Ni xix	12.430	12.437(.015)	0.08(.04)	0.13
Fe xx	12.654	12.662(.022)	0.07(.04)	0.11
Fe xx	12.818+.847	12.845(.009)	0.25(.05)	0.39
Fe xx	12.946+.978	12.973(.014)	0.12(.04)	0.18
???	—	13.257(.016)	0.10(.04)	0.16
Ne ix	13.447	13.450(.006)	1.45(.15)	2.15
Ne ix	13.553	13.542(.007)	1.10(.14)	1.61
Ne ix	13.700	13.723(.011)	0.27(.05)	0.39
Fe xvii	13.823	13.824(.009)	0.42(.06)	0.60
Ni xix	14.040+.081	14.052(.008)	0.31(.05)	0.43
Fe xviii	14.202+.255	14.209(.005)	0.76(.11)	1.06
Fe xviii	14.344+.361	14.364(.008)	0.34(.05)	0.48
Fe xvii	15.015	15.011(.002)	2.54(.11)	3.36
O viii	15.176	15.175(.012)	0.50(.10)	0.64
Fe xvii	15.260	15.264(.008)	1.03(.11)	1.34
???	—	15.844(.013)	0.20(.12)	0.24
O viii	16.007	16.002(.006)	0.89(.11)	1.11
Fe xvii	16.073	16.092(.014)	0.34(.09)	0.42
Fe xvii	16.229	16.220(—)	≤ 0.07	0.08
Fe xix	16.284	16.296(.020)	0.06(.03)	0.07
Fe xvii	16.777	16.775(.003)	1.39(.09)	1.62
Fe xvii	17.054	17.054 ^e	2.48(.18)	2.89
Fe xvii	17.097	17.097 ^e	1.02(.16)	1.18
O vii	17.768	17.763(.012)	0.16(.05)	0.18
O vii	18.627	18.628(.008)	0.58(.07)	0.62
O viii	18.969	18.968(.002)	6.60(.18)	6.91
N vii	20.910	20.894(—)	0.06(—)	0.05
O vii	21.602	21.614(.003)	6.29(.24)	5.81
O vii	21.804	21.793(.003)	5.57(.23)	5.07
O vii	22.101	22.101 ^e	0.25(.09)	0.22
Ca xiv+S xiv	24.133+.285	24.167(.056)	0.26(.11)	0.21
N vii	24.781	24.788(.011)	1.38(.15)	1.11
Ar vii	25.684	25.705(.030)	0.46(.12)	0.36
C vi	26.357	26.356(—)	0.26(—)	0.20
C vi	26.990	26.990(.047)	0.30(.13)	0.23
C vi	28.466	28.462(.017)	0.57(.15)	0.40
N vi	28.787	28.763(.028)	1.27(.20)	0.88
N vi	29.084	29.065(.037)	0.86(.18)	0.58
N vi	29.534	29.475(.060)	0.36(.14)	0.24

blends are taken into account. From that point on the same procedure was used as in Sect. 4: a Gaussian was folded through the response matrix and fitted to the line profiles of each ion line individually. The line flux ratios (f/i) obtained in this way are collected in Table 6. They might differ from ratios derived from Table 3, as in that table total feature fluxes, polluted by blends and satellite lines are given with their dominant identifications.

ion	λ_0^a [Å]	λ_{obs}^b [Å]	flux ^c	flux ^d
C vi	33.736	33.728(.008)	4.88(.39)	2.88
Ca xi	35.212	35.175(.078)	0.53(.18)	0.30
Ca xi	35.576	35.580(.054)	0.62(.18)	0.35
S xii	36.563+.398	36.500(.036)	0.74(.20)	0.40
Si xiii+S xi	37.786+.773	37.787(.040)	0.83(.23)	0.43
S xi	39.240+.323	39.234(.036)	1.43(.29)	0.72
C v	40.268	40.240(.020)	2.74(.74)	1.35
C v	40.729	40.730 ^e	1.96(.53)	0.97
C v	41.472	41.474(.024)	0.66(.32)	0.32
Mg x+Si xii	44.050+.020	44.031(.022)	0.85(.13)	0.39
Si ix+xii	44.249+.165	44.265(.017)	0.92(.13)	0.41
Si xii	45.520+.680	45.533(.033)	0.20(.09)	0.09
Si xi	46.300+.410	46.308(.062)	0.42(.11)	0.18
Mg x+S ix	47.280+.500	47.410(.050)	0.58(.12)	0.24
Ar ix+Si xi	49.180+.220	49.165(.025)	1.10(.16)	0.44
Si x	50.254+.305	50.284(.015)	1.07(.21)	0.42
Si x	50.524+.691	50.545(.031)	1.21(.20)	0.48
Si x	52.1784+.248	52.232(.038)	0.72(.22)	0.28
Fe xv+Si ix	52.911+.834	52.838(.044)	1.04(.24)	0.39
Fe xvi	54.710	54.700(.045)	0.72(.19)	0.26
Si ix	55.356+.272	55.340(.028)	1.50(.22)	0.54
Fe xv	59.404	59.350(.103)	0.38(.15)	0.13
???	—	60.003(.078)	0.40(.15)	0.13
Si ix+xiii	61.050-.84	61.416(.087) ^f	1.90(.14)	0.61
Si ix+xii	68.148+.548	68.328(.081)	0.70(.22)	0.20
Si viii	69.825	69.812(.055)	0.81(.21)	0.23

Notes:

a: λ_0 are the theoretical wavelength values from Kelly (1987).

b: λ_{obs} is the observed wavelength with the statistical 1σ error in parentheses.

c: in units 10^{-4} photons $\text{cm}^{-2}\text{s}^{-1}$

d: in units 10^{-13} ergs $\text{cm}^{-2}\text{s}^{-1}$

e: wavelength fixed at theoretical values

f: broad line

Table 4. Higher-order lines and their line fluxes in the spectrum of δ Ori.

ion	λ_0^a [Å]	λ_{obs}^b [Å]	$\lambda_{\text{obs}}/\text{order}$ [Å]	flux ^c
Fe xvii	15.015	30.020(.012)	15.010(.006)	0.27(.09)
Ne ix	13.447+.553	40.545(—)	13.515(—)	1.12(—)
Fe xvii	15.015	45.004(.026)	15.001(.009)	0.47(.10)
Fe xvii	17.054+.097	51.204(.067)	17.068(.022)	0.50(.17)
O viii	18.969	56.936(.030)	18.978(.010)	1.79(.24)
O vii	21.602+.804	65.171(.165)	21.724(.055)	1.86(.52)
C vi	33.736	101.222(.348)	33.741(.116)	2.02(.88)

Notes:

a: λ_0 are the theoretical wavelength values from Kelly (1987).

b: λ_{obs} higher-order observed wavelength with the statistical 1σ error in parentheses.

c: in units 10^{-4} photons $\text{cm}^{-2}\text{s}^{-1}$.

The line flux ratios are compared with those given by Miller et al. (2002) using *HETGS*. Their values and ours are in good agreement. The ratios have been applied to a Planck UV-radiation field of 33000 K at the wavelengths of the $1s2s^3S - 1s2p^3P$ transitions of the corresponding ions, in combination with scaled formulas given by Blumenthal et al (1972). This UV radiation field de-

Table 6. He-like and H-like over He-like line flux ratios and corresponding distances in R_* and temperatures. Values obtained by Miller et al (2002) are also given.

this work		Miller et al. 2002	
ion	f/i	distance(R_*)	f/i
C v	0.31(.10)	75(14)	—
N vi	0.38(.17)	49(13)	—
O vii	0.052(.016)	9.0(1.5)	$\lesssim 0.2$
Ne ix	0.10(.06)	3.4(1.1)	$\lesssim 0.1$
Mg xi	0.73(.48)	3.2(1.4)	0.5(.4)
Si xiii	$\lesssim 0.6$	—	2.2(1.5)
ion	$(f+i)/r$	T(MK)	$f+i/r$
C v	0.96(.34)	1.0	—
N vi	0.86(.23)	1.6	—
O vii	0.93(.06)	1.7	0.78(0.35)
Ne ix	0.94(.14)	2.3	1.09(0.44)
Mg xi	1.08(.37)	2.1	0.54(0.28)
Mg xii ^a	0.81(.23)	4.4	—
Si xiii	0.69(.27)	8.0	0.84(0.34)
Si xiii ^a	0.77(.22)	6.4	—
ion	$r_H^2/(r+i+f)$	T(MK)	
C vi/v	0.91(.18)	1.18(0.07)	
N vii/vi	0.55(.09)	1.64(0.08)	
O viii/vii	0.55(.02)	2.44(0.02)	
Ne x/ix	0.35(.04)	3.8(0.1)	
Mg xii/xi	0.24(.09)	6.0(0.5)	
Si xiv/xiii	0.22(.14)	9.4(1.3)	

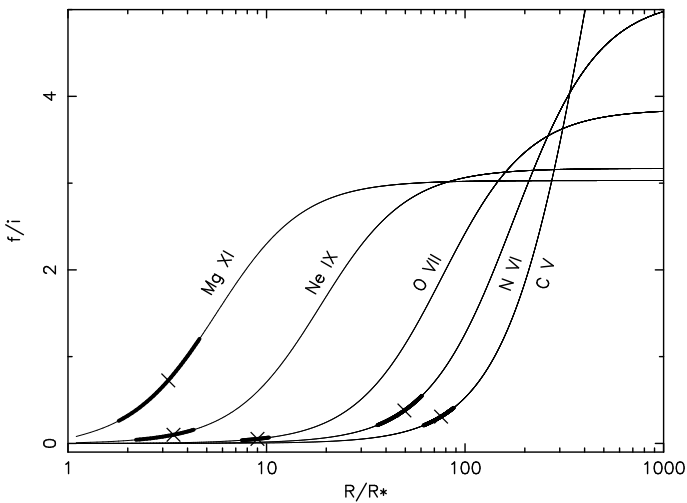
Notes:

a: Average of our value and the *HETGS* value obtained by Miller et al. (2002)b: r_H is the line flux for the H-like resonance line doublet

creases with distance from the stellar surface by a dilution factor:

$$W(r) = \frac{1}{2} \left[1 - \left(1 - \left(\frac{R_*}{r} \right)^2 \right)^{1/2} \right]. \quad (1)$$

As a result of the radial dependence of the radiation field, the observed f/i ratio can be used to derive the radial location of the He-like ions that are producing the observed *fir* lines.

**Fig. 4.** The f/i ratio versus the distance to the stellar surface in stellar radii (R_*).

The influence of the UV radiation field on the population of the $1s2s\ ^3S_1$ and $1s2p\ ^3P_1$ levels is reflected in the f/i ratio, hence in the distance to the stellar surface as shown in Fig. 4. The shapes of the curves are the same as those given by Miller et al. (2002) for Mg xi, Ne ix, and O vii. The curves of N vi and C v are new and established as a result of our investigation. The bold intervals on the trajectory show the average distance from the stellar surface (including the 1σ statistical error) where the ion is formed. From this figure it is clear that the hotter ions (Mg xi and Ne ix) are formed closer to the stellar surface than the cooler ones (C v and N vi). In the short wavelengths our results are in good agreement with Fig. 4 in the paper by Miller et al. (2002) and with the values of Mg xi and O vii by Waldron & Cassinelli (2007), based on *HETGS* observations. At the longer wavelengths, N vi and C v (outside the *HETGS* range) show that the X-rays are formed much farther out in the wind than the wind acceleration zone, which stops at about $10 R_*$. The N vi is located at $49(13)R_*$ and C v at $75(14)R_*$ with temperatures of 1.6 MK and 1.0 MK respectively (see Table 6).

Only an upper value has been determined for Si xiii. This feature is better imaged by *HETGS*, and therefore the distance of its plasma to the stellar surface is excluded from Table 6 and Fig. 4. Also included in Table 6 are the temperature indicators $G = (f+i)/r$ of the He-like ions, as well as the ratios of the H-like resonance lines and the He-like line triplets. They result in temperatures for the X-ray emitting plasma, related to the location of the specific ions in the plasma.

5. Multitemperature fitting

Along with the individual line analysis we investigated the *LETGS*-spectrum of δ Ori using a multithermal model for optically thin plasma in CIE as implemented in SPEX (Kaastra et al. 1996a) in combination with MEKAL (Mewe et al. 1985, 1995; Kaastra et al. 1996b)³. It provides a calculation with thousands of lines and a model electron continuum. The ionization equilibrium is based on calculations by Arnaud & Rothenflug (1985) and Arnaud & Raymond (1992), the latter especially for iron. Application of a non equilibrium ionization model did not improve the description of the spectrum.

The fits were applied using the C-statistics approach. For the transition probabilities of the model line features, an uncertainty of 15% was assumed, a value that accords with the *NIST* database⁴. The first calculation was fitted to the data, taking the errors on the data count rate into account. In the follow up of the fitting procedure the errors on the model count rate were applied to avoid over-influences of incidental low count rate bins.

5.1. A 3-T model

We started the fitting procedure with more fixed temperature components, out of which only three components were significant. From that point on a three temperature (3-T) fit was applied for the CIE-model. The values of the fit are collected in Table 7. This table shows the interstellar column density N_H , the obtained temperatures, the emission measures, the luminosities of the different temperature bins, absorption column densities for the three temperature components in the wind, abundances, line shifts (z), and line broadening (v_{mic}).

³ <http://www.sron.nl/SPEX>⁴ <http://www.nist.gov/pml/data/asd.cfm>

Table 7. The 3-T fit to the *LETGS* spectrum of δ Ori, applying a CIE-model to the total (time) spectrum. The distance is put at 112 pc (Van Leeuwen 2007).

Parameters	
model	
$\log N_H [\text{cm}^{-2}]$	20.18(.03)
z (Redshift)	-2.3(.5)e-4
v_{mic}	1039(21)
T_1 [keV]	0.098(.005)
T_2 [keV]	0.228(.008)
T_3 [keV]	0.647(.010)
$EM_1 [10^{54} \text{cm}^{-3}]$	2.05(.20)
$EM_2 [10^{54} \text{cm}^{-3}]$	2.27(.09)
$EM_3 [10^{54} \text{cm}^{-3}]$	0.88(.04)
$L_1 [10^{31} \text{erg/s}]^a$	7.10
$L_2 [10^{31} \text{erg/s}]$	5.14
$L_3 [10^{31} \text{erg/s}]$	2.59
$L_{Tot} [10^{31} \text{erg/s}]$	14.83
$Nh_1 [10^{20} \text{cm}^{-2}]$	0.21(.16)
$Nh_2 [10^{20} \text{cm}^{-2}]$	1.52(.37)
$Nh_3 [10^{20} \text{cm}^{-2}]$	26.7(4.0)
C	1.080(.016)
N	1.046(.020)
O	0.859(.009)
Ne	1.243(.015)
Mg	1.650(.022)
Si	0.913(.012)
Fe	1.000(fix)
$C - \text{stat/d.o.f.}$	2836/1609
$C - \text{stat}_{red}$	1.76

a : In the range from 0.07 to 3 keV. (*LETGS* band).

Three statistically well-determined temperature components at 0.10, 0.23, and 0.65 keV have been established. The two coolest components correspond to the lines of the He-like ions, discussed in Sect. 4. According to conclusions from that section, the hottest component (0.65 keV), that is responsible for Si xiv and S x v is formed deeper in the wind.

The results of the total 3-T fit to the spectrum are shown in Fig. 5. The lines and continua from the three individual temperature components are shown in the three top panels of Fig. 6. The bottom panel shows the data with the calculated continuum as sum of the three continua of these components.

The tabulated emission measure is defined as

$$EM = n_e n_H V, \quad (2)$$

in which $n_H = 0.85 n_e$.

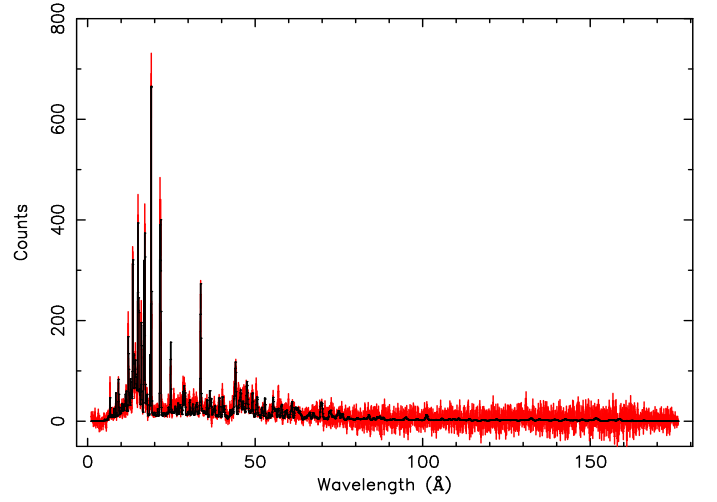
Knowledge of the electron density offers the possibility to calculate the X-ray emitting volume. The electron density for hot stars with a spherically symmetric stellar wind can be obtained via the following continuity equation:

$$\dot{M} = 4\pi R^2 \rho(R) V(R). \quad (3)$$

In this formula \dot{M} is the mass loss rate ($1.07 \times 10^{-6} M_\odot$ /year (Lamers & Leitherer 1993)) for δ Ori, R is the distance from the stellar surface, $\rho(R)$ the density at distance R , and $V(R)$ the wind velocity at distance R , related to the terminal velocity (V_∞) by

$$V(R) = V_\infty \times (1 - R_*/R)^\beta, \quad (4)$$

in which β is a coefficient between 0.85 for subgiants and 1.1 for supergiants. We use a value of 1.0 for β .

**Fig. 5.** The spectrum of δ Ori (red/gray), together with the model (black) derived from the multitemperature fit applying the parameters given in Table 7.

The InterStellar Medium (ISM) N_H was fitted and found to be $1.5 \times 10^{20} \text{cm}^{-2}$. Three additional wind absorption parameters were applied using the hot module in *SPEX*. It describes a warm plasma, as the CIE-model, while calculating the continuum absorption, as well as the line absorption. Emission lines with the highest oscillator strength are mostly influenced. The temperatures of this hot plasma were coupled to the temperatures of the components in the CIE-model. The hottest component, which is formed deeper in the wind (see Sect. 4), results in the highest absorption column density. No absorption for the cool wind (33000 K) could be determined. This implies that the overall cool stellar wind absorption is not taken into account and might have been taken over partly by the fitted ISM-parameter N_H .

A slight shift in λ ($\approx -2.3\text{e-}4$) was applied to optimize the fitted wavelengths. A line broadening parameter v_{mic} of 1039 km/s was added and fitted to the overall spectrum to take into account the broadening of the line features. The HWHM of a line is related to the v_{mic} by the following formula (see also Sect. 3):

$$HWHM/\lambda_{obs} = \frac{\sqrt{\ln 2} v_{mic}}{c}. \quad (5)$$

The X-ray luminosities of the three individual temperature components are given over the LETG energy range from 0.07 to 3.0 keV. For the luminosities no individual statistical errors have been determined. Their uncertainties are supposed to have the same relative values as those for the emission measures because the luminosity is mostly determined by the emission measures in this temperature range, and therefore $L_X \propto EM$. The total luminosities (summed over the three temperature components) in other energy bands (0.5-4 keV, 0.1-2.4 keV, and 0.4-4 keV) for *Einstein*, *ROSAT*, *ASCA* given in the papers by Cassinelli & Swank (1983), Haberl & White (1993), and Corcoran et al. (1994), respectively, do agree with our values when taking differences in interstellar absorption or distance into account.

The abundances are relative to solar photospheric values (Lodders et al. 2009). The absolute values of the abundances are strongly influenced by the obtained values of the emission measures. The product of abundances and emission measures ($A \times EM$), however, is the robust quantity for the line spectrum, therefore, abundance-ratios are often given relative to an abundant element in the stellar atmosphere. Here the abundance of iron was

fixed at its solar photospheric value. The abundance values agree with the value of ≈ 0.9 that Simón-Díaz (2010) finds for oxygen and silicon abundances in the Orion star-forming region.

A fit to the spectrum taken by *HETGS* applying the same set of parameters needs a lower value for v_{mic} (see also Sect. 3). This might be due to inconsistency between the LSFs of the used instruments. Also the description of the Si XIII and Si XIV line features is not satisfactory. This might be because these features are near the end of the calibrated area for both instruments.

To investigate the time dependence of the spectrum, as suggested by the light curve (see Fig. 1) we split the observation into two time intervals, 0-49 ks and 49-98 ks. The emission measure of the hottest component (formed closest to the stellar surface) is about 10% lower in the first time interval than in the last 49 ks. This might agree with some eclipsing by the companion star.

5.2. DEM modeling

To show the smooth connection between the separated temperature bins, we performed a continuous DEM-modeling for the spectrum of δ Ori by applying the regularization method (Kaastra et al. 1996b) in the SPEX-code. This method uses direct matrix inversion with the additional constraint that the second-order derivative of the solution with respect to the temperature is as smooth as possible. In this DEM modeling the abundances given in Table 7 have been used. The results are shown in Fig. 7.

The results of the fits, collected in Table 7 and Fig. 7, are in good agreement. The peak of our DEM agrees with the peaks found by Miller et al. (2002) and Wojdowski & Schulz (2005). However, our DEM extends more to lower temperatures and their values extend further to higher temperatures as a consequence of using two different instruments. The peak value given by Wojdowski & Schulz (2005) is higher.

As for the CIE-fit we also performed a DEM-modeling for the partial spectra of 0-49 ks and 49-98 ks, again applying the regularization method. These two DEM-modelings are shown in Fig. 8. Although the hottest component is again a bit stronger for the last 49 ks, no significant difference can be established between fits to the partial spectra.

6. Discussion and conclusions

The X-ray spectrum of the O-star δ Ori obtained with *LETGS* is rich in lines belonging to H-like and He-like ions of C, N, O, Ne, Mg, and Si. A weak He-like (S XV) triplet is also present. Other possible weak features present below 5 Å fall outside the calibrated bandwidth of the *LETGS*. Iron L-shell lines are dominant. The Ne-like transitions, between electron configurations of an inert noble gas, are favored for iron (Fe XVII) as well as for calcium (Ca XI), and nickel (Ni XIX).

Above 50 Å a few new line features were identified, some of which are third-order lines associated with strong first-order features located between 15 and 35 Å. No lines of cool ions were detected at wavelengths higher than 70 Å. The main reasons for the absence of these line features is the absence of a noticeable volume of cool (0.05 keV) plasma and the interstellar absorption.

Based on the forbidden line over intercombination line ratio in He-like ions the average distance of the X-ray emitting plasma to the stellar surface has been determined. Depending on the ion (temperature), the plasma emitting region is between 2 and 80 R_* for ions from Mg XI to C V. The cooler plasma (lower ionization stages) is located farther out in the wind. For the hot ions, Mg XI, Ne IX, and O VII, the average X-ray emitting plasma is from 2

to 10 R_* , respectively. This is in accordance with observations by Waldron & Cassinelli (2007) and Miller et al. (2002) using *HETGS*. Using *LETGS* that extends to longer wavelengths, the cooler ions N VI and C V have been observed as part of this investigation. The X-rays from these ions are formed on average at 50 R_* and 75 R_* , respectively, much farther out in the wind than the acceleration zone, where the final velocity has been reached. Here the wind is expected to be steady. However, small deviations in velocity (weak shocks) will be able to produce the cooler ions.

The spectrum is described well by a CIE model. Three well-distinguished temperature components have been determined: 0.10, 0.23, and 0.65 keV. The first two are in good agreement with the two temperatures found by Haberl & White (1993). They did not determine a third temperature component. The two lower temperature components (0.098 and 0.228 keV) describe the line-forming regions of the cooler ions, N VI and C V, and the moderately ionized species Mg XI, Ne IX, O VII, and O VIII, respectively, while the hottest component is supposed to produce even hotter ions deeper in the wind and a hot continuum.

Three emission measures are established, related to the obtained temperatures. Knowledge of the electron density offers the possibility to calculate the X-ray emitting volume. Applying the distances (see Table 6 and Fig. 4) and the wind velocity and density formulas 4 and 5, given in Sect. 5.1, we have calculated the electron densities for the regions where the specific ions produce X-ray radiation.

Because the distances given in Table 6 and Fig. 4 are average values with the statistical error on this average and not the limits of the X-ray emitting distance, it is difficult to calculate the total wind volume in which the conditions are optimal for the corresponding He-like ion emission. By assuming a wind volume from half to twice the obtained average distance we get the percentage of the wind that contributes to that ion. The emitting volumes are about 1% of the wind volume for the cooler plasma and less for the hotter ions.

The N_H of the ISM is mainly based on the long wavelength part of the spectrum. Its value of $1.51(06) \times 10^{20} \text{ cm}^{-2}$ is in good agreement with the value of $1.56 \times 10^{20} \text{ cm}^{-2}$ found by Jenkins et al. (1999) based on 57 IUE observations, and slightly lower than the value found by Haberl & White (1993) for their $T=0.1$ keV component. Additional wind absorption column densities have been determined (see Table 7). They are related to the temperature components of 0.10, 0.23, and 0.65 keV, with distances to the stellar surface of about 60 R_* , 6 R_* , and 2 R_* , respectively, where the plasma is formed on average. In combination with formula 4 we calculated that about 7% of the wind contributes to the hot wind absorption. No absorption of the overall cool stellar wind could be determined. This means that this absorption component is not explicitly taken into account during the fitting procedure. However, the effect might have been taken over by the other absorption parameters.

The X-ray luminosities of the three temperature components in the total *LETGS* band (0.07-3 keV) are 7.10, 5.14, and $2.59 \times 10^{31} \text{ erg/s}$. Two partial spectra were derived: one from the first 49 ks and another from the last 49 ks of the observation. This division was suggested by the light curve (see Fig. 1). No significant differences between the spectra, their temperature structures, their line shapes, or line fluxes have been established.

The obtained abundances are relative to solar photospheric values (Lodders et al. 2009). They were fit by fixing the iron abundance at its solar photospheric value and leaving the carbon, nitrogen, oxygen, neon, magnesium, and silicon abundances free to vary. Fixing the iron abundance was done because the abun-

dances and emission measures are strongly anticorrelated, especially in spectra with a weak continuum to establish the emission measure. The obtained values for oxygen and silicon are in good agreement with values found by Simón-Díaz (2010) in the Orion star-forming region.

The lines are symmetric and their HWHMs are about 840 km s^{-1} , far below the terminal velocity of 2000 km s^{-1} , but higher than the values found by Miller et al. (2002) using *HETGS*. This might be due to inconsistencies between the instrumental line spread functions in the calibration files of *HETGS* and *LETGS*. The ultimate velocities, measured at the end of the wings, are about 1850 km s^{-1} with an uncertainty of 200 km s^{-1} .

The measured line shifts given in Table 5, as well as the z -value given in Table 7, indicate that the velocity of the radiative plasma in the direction from or to the observer is low. This is well known for OB stars, especially among giants and supergiants (Waldron & Cassinelli 2007).

The conclusion should be that the radiation we observe is produced in plasma that has a very low velocity or moves perpendicular to the line of sight. There might be several explanations. The clumps, which collide with the wind and produce the X-ray radiation, have low velocities. In that case the relative velocity of the clumps to the wind is highest far out in the wind at terminal wind velocity. As a consequence the highest stages of ionization are produced far out in the wind, which contradicts our observation based on the forbidden-to-intercombination line ratios in He-like ions (see Fig. 4). Additionally, after the acceleration phase one does not expect velocity differences that are too high. The secondary star and its wind play important roles in the explanation of the δ Ori spectrum. However, this is discussed by Miller et al. (2002) and rejected. A third option is that the clumps screen their own X-ray radiation when they are in between the star and the observer. Only when the wind-clump collision is almost perpendicular to the line of sight is the radiation observable and spread over a narrow velocity range as derived from the HWHM. The effects of clumping and porosity on X-Ray emission-line profiles from hot-star winds have been described extensively by Owocki & Cohen (2006) and Oskinova et al. (2006).

Acknowledgements. The SRON National Institute for Space Research is supported financially by NWO.

References

- Arnaud, M., & Raymond, R. 1992, *ApJ*, 398, 394
 Arnaud, M., & Rothenflug, J. 1985, *A&AS*, 60, 425
 Berghöfer, T.W., Schmitt, J.H.M.M., & Cassinelli, J.P. 1996, *A&AS*, 118, 481
 Blumenthal, G.R., Drake, G.W.F., & Tucker, W.H. 1972, *ApJ*, 172, 205
 Cassinelli, J.P., & Swank, J.H. 1983, *ApJ*, 271, 681
 Cassinelli, J.P., Waldron, W.L., Sanders, W.T., et al. 1981, *ApJ*, 250, 677
 Cohen, D.H., Leutenegger, M.A., Grizzard, K.T., et al. 2006 *MNRAS*, 368, 1905
 Corcoran, M.F., Waldron, W.L., MacFarlane, J.J., et al. 1994, *ApJ*, 436, L95
 Dessart, L., & Owocki, S.P. 2005, *A&A*, 437, 657
 Gabriel, A.H., Jordan, C. 1969, *MNRAS*, 145, 241
 Haberl, F. & White, N. 1993, *A&A*, 280, 519
 Harnden, F.R., Branduardi, G., Elvis, M., et al. 1979, *ApJ*, 234, L51
 Harvey, A.S., Stickland, D.J., Horwarth, I.D., & Zuiderwijk, E.L. 1987, *Observatory*, 107, 205
 Harvin, J.A., Gies, D.R., Bagnuolo, W.G., et al. 2002, *ApJ*, 565, 1216
 Jenkins, E.B., Tripp, T.M., Woźniak, P.R., Ulysses, J.S., & Sonneborn, G., 1999, *ApJ*, 520, 182
 Kaastra, J.S., Mewe, R., & Nieuwenhuijzen, H. 1996a, in: K. Yamashita & T. Watanabe (eds.), *UV and X-ray Spectroscopy of Astrophysical and Laboratory Plasmas* (Tokyo: Universal Academy Press, Inc.), p. 411 (SPEX)
 Kaastra, J.S., Mewe, R., Liedahl, D.A., et al. 1996b, *A&A*, 314, 547
 Kahn, S.M., Leutenegger, M.A., Cottam, J., et al. 2001, *A&A*, 365, L312
 Kelly, R.L. 1987, *J. Phys. Chem. Ref. Data*, 16, Suppl. 1
 Lamers, H.J.G.L.M. & Leitherer, C. 1993, *ApJ*, 412, 771
 Leutenegger, M.A., Paerels, F.B.S., Kahn, S.M., & Cohen, D.H. 2006, *ApJ*, 650, 1096
 Lodders, K., Palme, H., & Gail, H.-P., 2009, *Landolt-Bornstein, New Series, Astronomy and Astrophysics*, Springer Verlag, Berlin (eprint arXiv:0901.1149)
 Lucy, L.B. 1982, *ApJ*, 255, 286
 Lucy, L.B., & White, R. 1980, *ApJ*, 241, 300
 Lucy, L.B., & Solomon, P.M. 1970, *ApJ*, 159, 879
 Mayer, P., Harmanec, P., Wolf, M., Božić, H., & Šlechta, M. 2010, *A&A*, 520, A89
 Mewe, R., Gronenschild, E.H.B.M., & van den Oord, G.H.J. 1985, *A&AS*, 62, 1 (MEKAL)
 Mewe, R., Kaastra, J.S., & Liedahl, D.A. 1995, *Legacy* 6, 16
 Miller, N.A., Cassinelli, J.P., Waldron, W.L., MacFarlane, J.J., & Cohen, D.H. 2002, *ApJ*, 577, 951
 Oskinova, L.M., Feldmeier, A., & Hamann, W.-R. 2006, *MNRAS*, 372, 313
 Owocki, S.P., & Cohen, D.H. 2006, *ApJ*, 648, 565
 Owocki, S.P., Castor, J.I., & Rybicki, G.B. 1988, *ApJ*, 335, 914
 Pollock, A.M.T., 2007, *A&A*, 463, 1111
 Raassen, A.J.J., van der Hucht, K.A., Miller, N.A., & Cassinelli, J.P., 2008, *A&A*, 478, 513
 Seward, F.D., Forman, W.R., Giacconi, R., et al. 1979, *ApJ*, 234, L55
 Simón-Díaz, S. 2010, *A&A*, 510, A22
 Tarasov, A. E., Harmanec, P., Horn, J., et al. 1995, *A&AS*, 110, 59
 Van Leeuwen, F. 2007, *A&A*, 474, 653
 Voels, S.A., Bohannon, B., Abbott, D.C., & Hummer, D.G., 1989, *ApJ*, 340, 1073
 Waldron, W.L., & Cassinelli, J.P. 2001, *ApJ*, 548, L45
 Waldron, W.L., & Cassinelli, J.P. 2007, *ApJ*, 668, 456
 Wilson, R.E. 1963, *General Catalogue Of Stellar Radial Velocities*, Carnegie Institution of Washington publication 601
 Wojdowski, P.S., & Schulz, N.S. 2005, *ApJ*, 627, 953

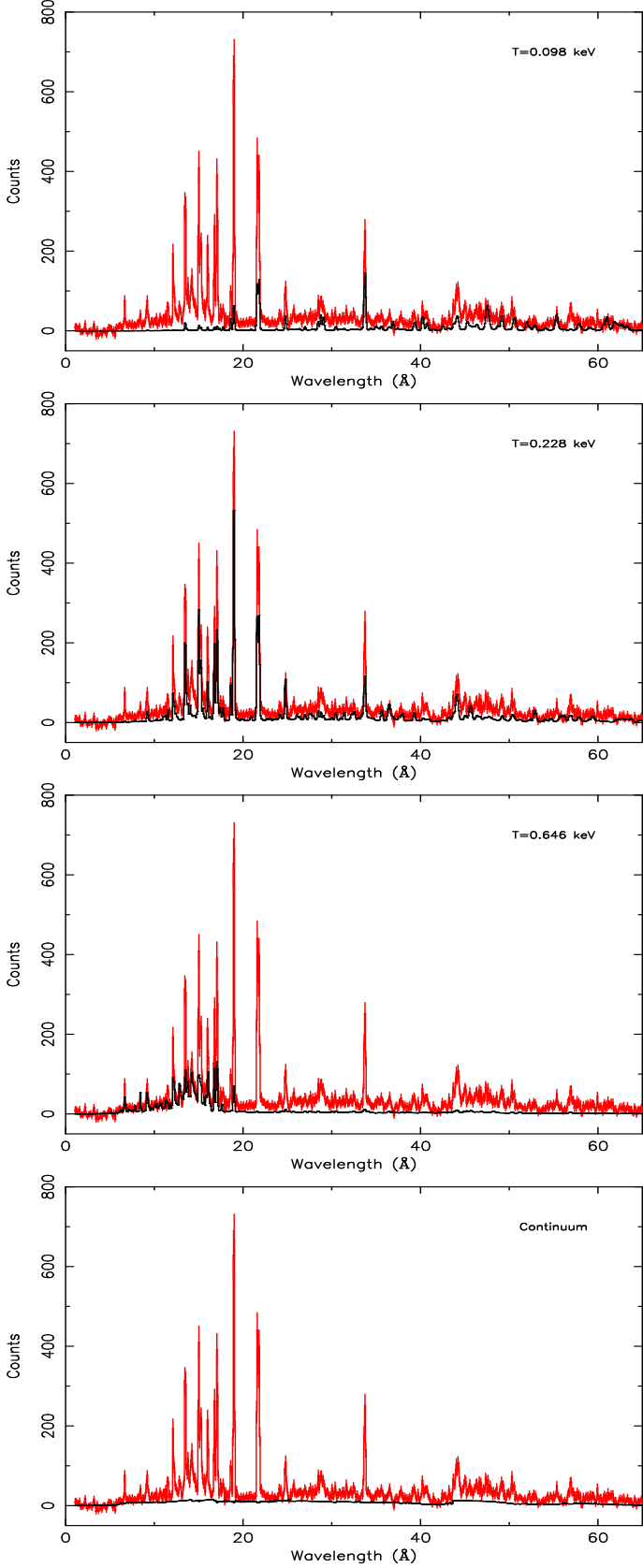


Fig. 6. The spectrum of δ Ori (red/gray), together with the three individual temperature contributions to the model (black), applying the parameters given in Table 7. They imply the line and continuum radiation from the individual components. The bottom panel shows the model electron continuum (black). This implies the sum of the three continua.

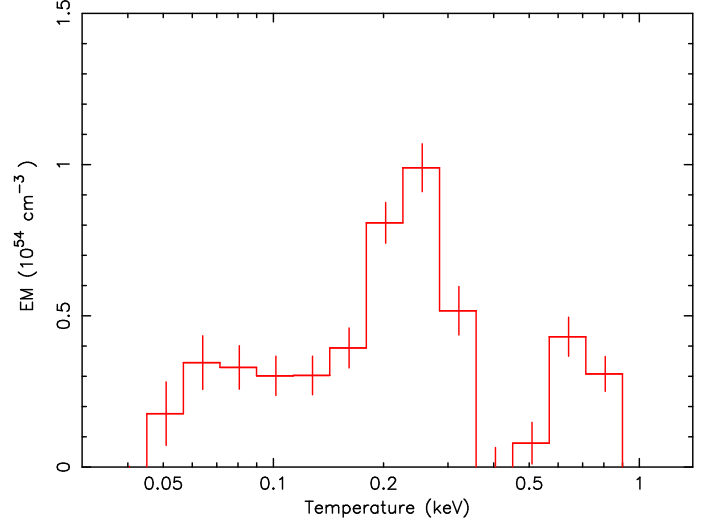


Fig. 7. DEM-modeling of δ Ori, based on the regularization method (Kaastra et al. 1996b) (see text). The EM is given in units of 10^{54} cm^{-3} .

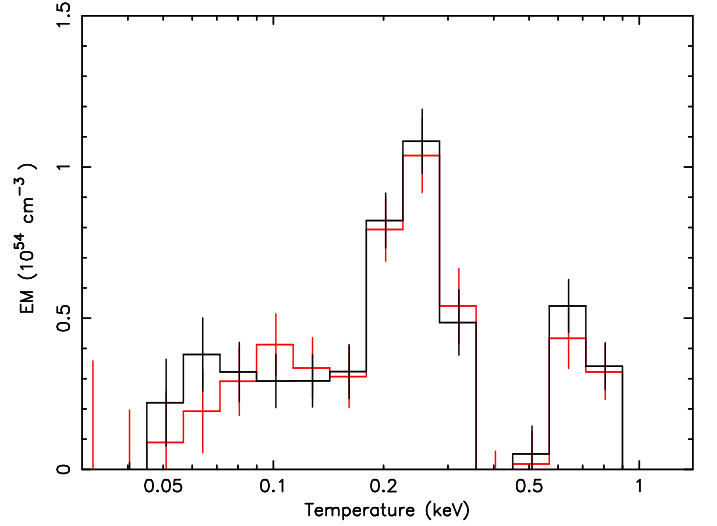


Fig. 8. DEM-modeling of δ Ori, based on the regularization method. The two DEMs show a modeling of the spectrum over the time interval 0-49 ks (red/gray) and 49-98 ks (black).

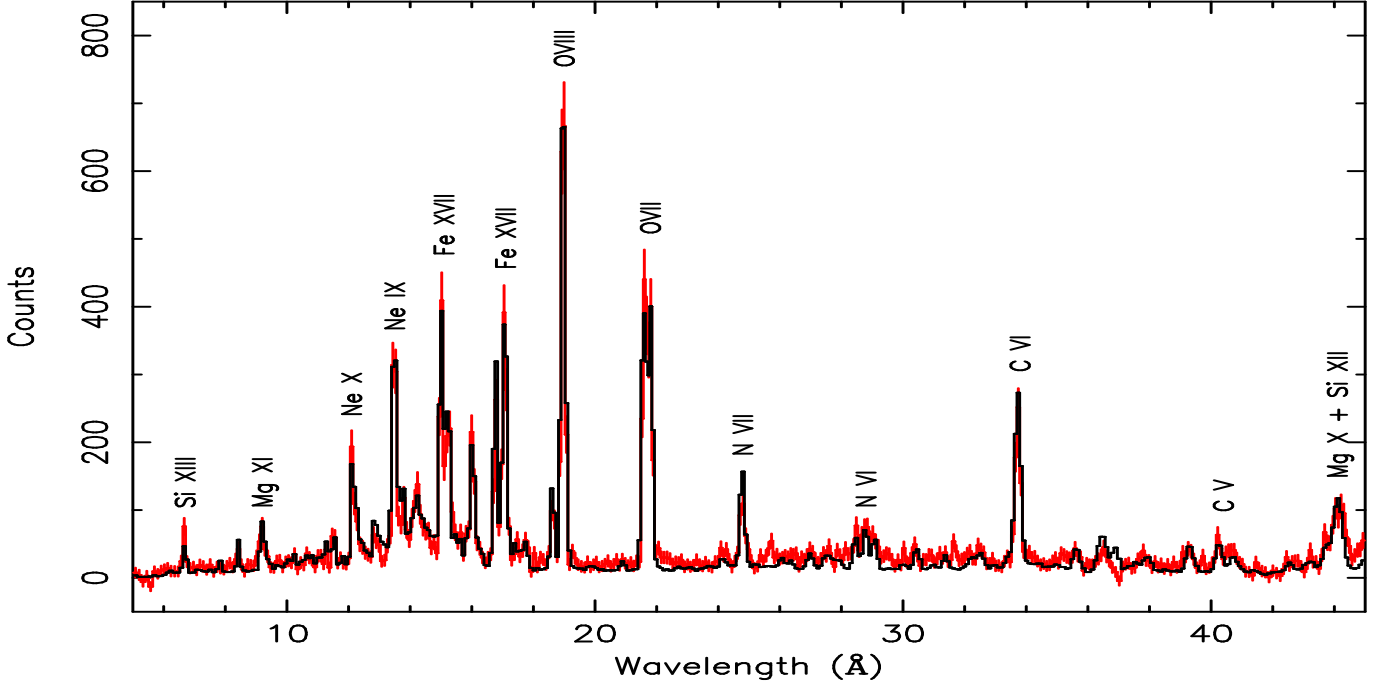


Fig. 3. Part of the spectrum of δ Ori. The most dominant lines are indicated. Data are in red (gray), the CIE-model in black)

Table 5. Wavelength shifts and half width at half maximum (HWHM) values for some strong isolated lines in the spectrum of δ Ori. The values have been compared with those from Miller et al. 2002.

ion	λ_0^a [Å]	λ_{obs} [Å]	$\Delta\lambda$ [Å]	shift in km s ⁻¹	shift(Miller) in km s ⁻¹	HWHM in km s ⁻¹	HWHM(Miller) in km s ⁻¹	blue wing in km s ⁻¹	red wing in km s ⁻¹
Ne x	12.134	12.1305(.0030)	-0.0035(.0030)	-87(74)	-150(100)	653(123)	420(170)	-1168	1246
Fe xvii	15.015	15.0100(.0023)	-0.0050(.0023)	-100(46)	-50(100)	840(80)	510(220)	-1734	1915
Fe xvii	16.777	16.7745(.0034)	-0.0025(.0034)	-45(57)	100(150)	853(89)	420(250)	-1804	1783
O viii	18.969	18.9684(.0015)	-0.0006(.0015)	-9(24)	60(100)	854(30)	700(100)	-2009	2067
O vii	21.602	21.6148(.0038)	0.0128(.0038)	178(53)	—	792(47)	—	-1808	1826
O vii	21.804	21.7930(.0041)	-0.0110(.0041)	-151(56)	—	812(61)	—	-1915	2066
N vii	24.781	24.7866(.0100)	0.0056(.0100)	68(121)	120(400)	750(169)	420(870)	-1704	1669
C vi	33.736	33.7252(.0050)	-0.0108(.0050)	-96(44)	—	835(55)	—	-1834	1751

Notes:

a: λ_0 are the theoretical wavelength values from Kelly (1987).